scientific reports

Check for updates

OPEN

A theoretical investigation of the effect of Ga alloying on thermodynamic stability, electronic-structure, and oxidation resistance of Ti₂AlC MAX phase

Daniel Sauceda[1], Prashant Singh[1,2]✉ & Raymundo Arroyave[1,3,4]

We present a systematic investigation of thermodynamic stability, phase-reaction, and chemical activity of Al containing disordered Ti₂(Al-Ga)C MAX phases using machine-learning driven high-throughput framework to understand the oxidation resistance behavior with increasing temperature and exposure to static oxygen. The A-site (at Al) disordering in Ti₂AlC MAX (M=Ti, A=Al, X=C) with Ga shows significant change in the chemical activity of Al with increasing temperature and exposure to static oxygen, which is expected to enable surface segregation of Al, thereby, the formation of Al₂O₃ and improved oxidation resistance. We performed in-depth convex hull analysis of ternary Ti–Al–C, Ti–Ga–C, and Ti–Al–Ga–C based MAX phase, and provide detailed contribution arising from electronic, chemical and vibrational entropies. The thermodynamic analysis shows change in the Gibbs formation enthalpy (ΔG_{form}) at higher temperatures, which implies an interplay of temperature-dependent enthalpy and entropic contributions in oxidation resistance Ga doped Ti₂AlC MAX phases. A detailed electronic structure and chemical bonding analysis using crystal orbital Hamilton population method reveal the origin of change in phases stability and in oxidation resistance in disorder Ti₂(Al₁₋ₓGaₓ)C MAX phases. Our electronic structure analysis correlate well with the change in oxidation resistance of Ga doped MAX phases. We believe our study provides a useful guideline to understand to role of alloying on electronic, thermodynamic, and oxidation related mechanisms of bulk MAX phases, which can work as a precursor to understand oxidation behavior of two-dimensional MAX phases, i.e., MXenes (transition metal carbides, carbonitrides and nitrides).

MAX phases are a family of layered ternary compounds with hexagonal symmetry, which get their ceramic and metallic properties from the alternatively arranged covalently bonded (M–X) and metallic (M–A) layers[1–5]. The high strength, good damage tolerance, machinability, exceptional thermal shock resistance, elastic stiffness, and thermal/electrical conductivity are equivalent to metal like high-temperature mechanical response, and outstanding ceramics like oxidation and corrosion resistance. Accordingly, there is a great interest in new MAX phases with improved properties like oxidation resistance. However, good oxidation resistance in crystalline materials requires the formation of protective oxidation layers. In high-temperature applications, the oxide phase formation depends heavily on the differences in the preparation process and atomic content. The MAX phases with significant Al, Cr, or Si, present in Ti₂AlC, Cr₂AlC, or Ti₃SiC₂ MAX phases, are known to enable good oxidation resistance through the formation of protective oxide layers, e.g., Al₂O₃, Cr₂O₃, or SiO₂, at high operating temperatures[6,7]. The atoms with metallic bonds in A-layer, e.g., Al/Cr/Si, are weaker compared to covalently bonded atoms in M (early transition metals)-X (group 13–16 element) layers. This results in smaller diffusion barriers for Al/Cr/Si atoms at A-sites, thereby, enabling the formation of protective oxides[6,8–13].

[1]Department of Materials Science and Engineering, Texas A&M University, College Station, TX 77843, USA. [2]Ames Laboratory, U.S. Department of Energy, Iowa State University, Ames, IA 50011, USA. [3]J. Mike Walker '66 Department of Mechanical Engineering, Texas A&M University, College Station, TX 77843, USA. [4]Wm Michael Barnes '64 Department of Industrial and Systems Engineering, Texas A&M University, College Station, TX 77843, USA. ✉email: psingh84@ameslab.gov; prashant40179@gmail.com

Ti$_2$AlC based MAX phases are projected as potential candidates for fuel coating and structural applications in nuclear (fusion and fission) reactors for their superior oxidation resistance properties[14–17]. Recently however, Sokol et al. has reported that Ti$_2$AlC does not provide a suitable protective coating against oxidation, while Cr$_2$AlC was found to produce a suitable oxidation barrier, i.e., an outstanding candidate[18]. Notably, the Ti$_2$GaC is another candidate material with remarkable electronic (phase stability and electronic-structure), structural (stability of crystal phases), and mechanical (exceptional thermal shock resistance and damage tolerance, excellent oxidation resistance, and elastic stiffness) properties[1,19–27]. Several ab-initio calculated MAX phase properties were found in good agreement with experiments[28–32], although high temperature studies of oxidation behavior of disordered Ti$_2$AlC/Ti$_2$GaC MAX phase are limited[33]. Therefore, it remains a challenge to understand the role of disorder and temperature on thermodynamic and oxidation resistance properties with respect to increasing exposure to oxygen. Furthermore, the chemical-disorder can significantly change the thermodynamic and oxidation behavior of MAX phases, altering the electronic structure properties of MAX phase. This suggests a strong connection of chemical disorder with electronic and thermodynamic properties[34–37].

In this work, we performed a detailed electronic-structure and thermodynamic analysis of Ti$_2$AlC MAX phases with a A(Al/Ga)-site disorder to provide mechanisms controlling oxidation behavior. To understand the overall oxidation process, we used a high-throughput framework comprised of a machine learning model and the grand-canonical linear programming (GCLP) method and analyzed the temperature-dependence of Gibbs formation enthalpy (ΔG_{form}) of Ti$_2$(Al$_{1-x}$Ga$_x$)C MAX phases. An in-depth thermodynamic analysis using convex hull of ternary Ti–Al–C, Ti–Ga–C, and Ti–Al–Ga–C based MAX phase was performed to provide detailed contribution arising from electronic, chemical and vibrational entropies. Our model is able to predict reaction products, phase-fractions, and chemical activities during the high-temperature reaction processes at given temperature and oxygen content. In general, the oxidation process can be attributed to the atomic interactions that arise from varying electronic states of different species that may enable or disable the formation of different kinds of oxides. Therefore, we systematically investigated the electronic-structures of series of Ga-doped Ti$_2$AlC MAX phases using ab initio methods to reveal the quantum mechanical origin of change in elemental chemical activity from alloying. To prove the charge effect on stability, we also performed chemical bonding analysis using crystal orbital Hamilton population (COHP) method. We believe that our study will guide experimentalists in understanding temperature dependent oxidation reaction processes in disorder MAX phases, exemplified for Ti$_2$(Al$_{1-x}$Ga$_x$)C MAX, which can be used to understand more complex MAX phases or even 2D MXenes.

Methods

Electronic-structure calculation.
The electronic-structure calculation was performed using density-functional theory method as implemented within Vienna Ab initio Simulation Package[38–40]. The Perdew–Burke–Ernzerhof (PBE) generalized gradient approximation (GGA) functional[41] was employed for geometrical and electronic relaxations of Ti$_2$(Ga$_x$Al$_{1-x}$)C MAX with total energy and force convergence criteria of 10^{-6} eV and 0.01 eV/Å. The Brillouin zone integration in ionic and charge self-consistency were performed on $6\times6\times2$ and $12\times12\times4$ k-mesh using Monkhorst–Pack method[42] with a plane-wave cutoff energy of 520 eV, where the effect of the core electrons and interaction between the nuclei and the valence was treated by the projector-augmented wave (PAW)[43,44]. Based on the work of Söderling et al.[45] and Giese et al.[46], we chose PBE was chosen over LDA or meta-GGA[47,48] exchange–correlation functionals, where it was shown that PBE provides accurate bonding properties, magnetic moments, and energetics comparing LDA or meta-GGA. The 128 atom random supercell with disorder at Al site (x = 0.25, 0.50, 0.75) in Ti$_2$(Ga$_x$Al$_{1-x}$)C MAX to avoid effect arising from cell size[49].

High-throughput machine-learning (SISSO) framework for oxidation analysis.
The machine-learning-based high-throughput method was used for assessing ΔG_{form}, phase-prediction, and chemical activity analysis of constituent elements of Ti$_2$(Ga$_x$Al$_{1-x}$)C MAX phase. The SISSO (Sure Independence Screening and Sparsifying Operator) trained machine-learning model[50] was integrated with grand-canonical linear programming (GCLP) method[51] into a single high-throughput framework[52,53]. The SISSO model uses DFT based formation enthalpy (ΔH_{form}) database to predict temperature dependent ΔG_{form} $[= \Delta H_{form} + \Delta G^{SISSO}(T) - \sum_i x_i \Delta G_i(T)]$[54,55], where $\Delta G^{SISSO}(T)$, $\Delta G_i(T)$, and x are vibrational (phonon) entropy, elemental energies, and the stoichiometric weight of each element in the compound, respectively. The ΔG_{form} also uses DFT-calculated ground state properties, including enthalpies of formation (ΔH_{form}) and volume. The ΔH_{form} of Ti–Al/Ga–C MAX phase was calculated as $E_{total}^{Ti2(Al-Ga)C} - \sum_i n_i E_i$, where $E_{total}^{Ti2(Al-Ga)C}$ is the total energy of the alloy, n_i is the number of atoms and E_i elemental energy of atom of type 'i'. The $\Delta G^{SISSO}(T)$ is estimated from machine learning trained Bartel model[56]:

$$G^{SISSO}(eV/atom) = \left(-2.48 \cdot 10^{-4} \cdot \ln(V) - 8.94 \cdot 10^{-5} \cdot mV^{-1}\right)T + 0.181 \cdot \ln(T) - 0.882,$$

where V is the volume calculated from the DFT and T is the temperature. The stable Ti–O, Al–O and Ga–O oxide phases were taken from NIST-JANAF database (experiments) for validation[54,57].

Grand canonical linear programming (GCLP).
The GCLP method was used to minimize the free energy of the mixture to identify equilibrium alloy phases:

$$\Delta G = \sum_P f_P \Delta G_P,$$

where the ΔG_P is the free-energy of competing crystalline phases, and f_P is the phase-fraction. The ΔG expression was used to minimize the free energy and predict favorable phases from Ti–Al–Ga–C + O$_2$ reactions.
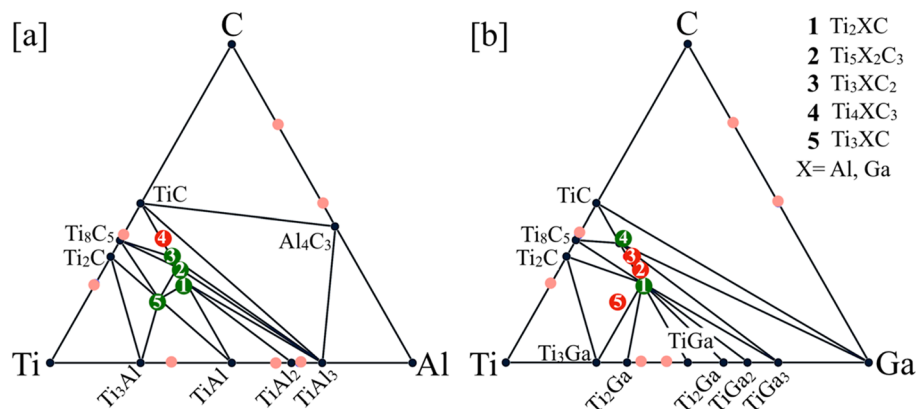
Figure 1. Ternary (**a**) Ti–Al–C, and (**b**) Ti–Ga–C convex hull based on experimentally known structures. The compositions marked as stable (green) and unstable (red) for given MAX phases[58]. The black and red (light) circles are stable and unstable binary/unary phases, respectively.

x (at. Frac.)	ΔG_{form} (eV/atom; T)			
	0 K	300 K	1000 K	1500 K
0.0	− 0.700	− 0.702	− 0.498	− 0.316
0.25	− 0.715	− 0.720	− 0.518	− 0.341
0.50	− 0.730	− 0.733	− 0.518	− 0.336
0.75	− 0.744	− 0.746	− 0.518	− 0.331
1.00	− 0.759	− 0.759	− 0.521	− 0.330

Table 1. The temperature dependent Gibb's formation enthalpy (E_{form}) of disorder $Ti_2(Al_{1-x}Ga_x)C$ MAX phases including the effect of chemical and vibrational entropy included through our machine learning framework.

The GCLP breaks down the alloy system into linear equations for given temperature and oxygen content. The OQMD (Open Quantum Materials Database) was used for ΔG, phase-fractions, and chemical activity prediction across the temperature range[54,55].

Results and discussion

Convex hull analysis for Ti$_2$AlC and Ti$_2$GaC.

We constructed the ternary Ti–Al–C and Ti–Ga–C convex hull based on experimentally stable and theoretically known[56] unstable phases in Fig. 1a,b. Notably, the coexistence of different phases occurs when a point lies on the simplex of the hull. The stable (green) and unstable (red) MAX phases including Ti_2XC, $Ti_5X_2C_3$, Ti_3XC_2, and Ti_4XC_3 are also marked the energies, and ΔG_{form} at 300 K, 1000 K, 1500 K are listed in Table 1. Other unary, binary, and ternary phases are marked. The stable phases lie on the connecting lines within convex hull formed between compounds and their elemental reference states[58,59]. The focus of our study is on the Ti_2XC MAX phases with 2:1:1 stoichiometry, interestingly, both Ti–Al–C (#1, Fig. 1a) and Ti–Ga–C (#1, Fig. 1b) has only 2:1:1 as common stable MAX phase.

Phase stability analysis of Ti$_2$(Al$_{1-x}$Ga$_x$)C MAX phase.

The Fig. 2a shows the formation energy (E_{form}) of $Ti_2(Al_{1-x}Ga_x)C$ calculated with the density-functional theory framework. Clearly, the increase in Ga at.% enhances the stability of $Ti_2(Al_{1-x}Ga_x)C$ with respect to pure Ti_2AlC MAX phase. In Fig. 2b, we show the temperature dependent Gibbs formation enthalpy (ΔG_{form}) of $Ti_2(Al_{1-x}Ga_x)C$ from 300 to 2000 K. At room temperature (RT), $Ti_2(Al_{1-x}Ga_x)C$ shows decrease in phase stability with increasing Al, where a crossover for Al cases at 800 K (x (Al) = 0, 0.25, 0.50, and 0.75 at.-frac.), energies are listed in Table 1. The ΔG_{form} shows weakly separated stability regions with respect to temperature at 800 K, i.e., below 800 K and over 800 K. The change in the ΔG_{form} at higher temperatures implies an interplay of temperature-dependent enthalpy and entropic contributions. This highlights the importance of temperature effect on ΔG_{form}, which is an important quantity that allows efficient determination of the most stable equilibrium state and can thus be used to assess the resulting reaction products for a given set of reactants[52].

Figure 3 shows the formation energy difference (ΔE_{form}) of $Ti_2(Al_{1-x}Ga_x)C$ were calculated within DFT method while temperature dependence was calculated ML framework[52]. The ΔG_{form} in Fig. 3 is plotted with respect to Ti_2GaC (x = 0) and Ti_2AlC (x = 1) MAX. Clearly, the increase in Ga at.% enhances the stability of $Ti_2(Al_{1-x}Ga_x)$ C, and the conclave slope in ΔG_{form} further confirms the mixing of Al–Ga on A-site. However, the ΔG_{form} with respect to end points (Ti_2GaC and Ti_2AlC) in Fig. 3 is very small at 300 K, i.e., increase in relative stability on Al doping does not change drastically. While increasing energy difference at higher temperatures (1000 K, 1500 K)
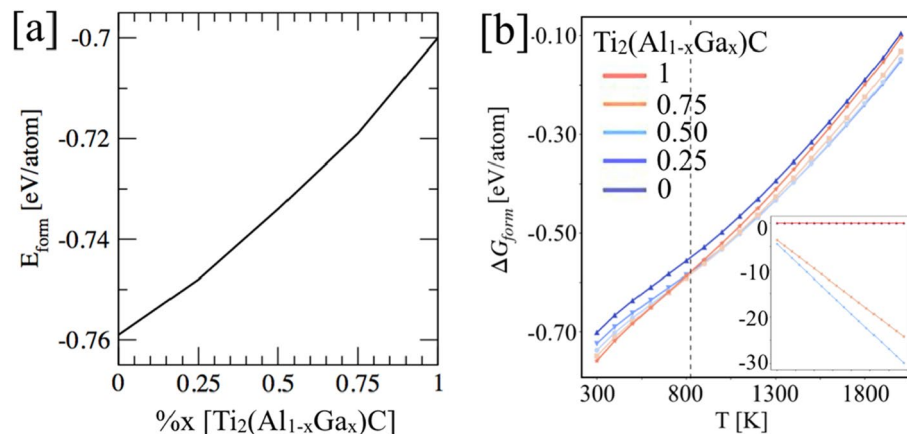
Figure 2. The density-functional theory predicted (**a**) formation enthalpy (0 K), and (**b**) relative phase stability of $Ti_2(Al_{1-x}Ga_x)C$ MAX phases with respect to constituent elements Ti, Al, Ga, and C. (**c**) The ML predicted temperature dependent ΔG_{form} (inset shows chemical entropy contribution to the disorder phase).
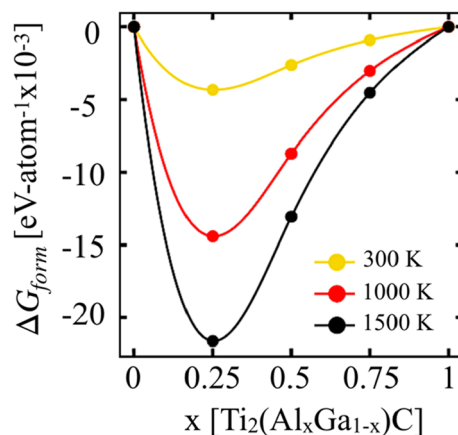

Figure 3. The ML predicted Gibbs formation enthalpies (ΔG_{form}) for $Ti_2(Al_{1-x}Ga_x)C$, x = 0, 1 atomic-fractions at 300 K, 1000 K, and 1500 K (see the ΔG_{form} in Table 1) with respect to Ti_2GaC (x = 0) and Ti_2AlC (x = 1).

x (at.-frac.)	Vol	E_{form} (0 K)	E_{el} (0 K)	E_{chem}			E_{vib}		
				300 K	1000 K	1500 K	300 K	1000 K	1500 K
0	14.02	− 0.700	− 0.0039	0	0	0	− 0.0693	− 0.3638	− 0.6565
0.25	13.98	− 0.715	− 0.0039	− 0.0036	− 0.0121	− 0.0182	− 0.0757	− 0.3852	− 0.6886
0.50	13.94	− 0.730	− 0.0038	− 0.0045	− 0.0149	− 0.0224	− 0.0760	− 0.3865	− 0.6904
0.75	13.90	− 0.744	− 0.0039	− 0.0036	− 0.0121	− 0.0182	− 0.0764	− 0.3877	− 0.6923
1.00	13.87	− 0.759	− 0.0041	0	0	0	− 0.0776	− 0.3916	− 0.6982

Table 2. The formation enthalpy and entropy contributions for $Ti_2(Al_{1-x}Ga_x)C$ MAX phases. The electronic entropy was calculated from DFT[38–40], the chemical entropy was estimated with relation $1/4(2 \times 0 + 1 \times (\sum_i c_i \ln c_i) + 1 \times 0)$, and vibrational contribution to entropy was predicted from Bartel Model[56] as implemented in our framework[52]. The volume and energy are in $Å^3$-atom^{-1} and eV-atom^{-1}, respectively.

show increasing lattice contribution as found in Table 2 (energies include electronic, chemical and vibrational entropy contributions)[52].

Model validation. The model evaluation is a very important criteria for the validation of theoretical predictions or framework, we calculate composition and temperature-dependent convex hull for Ti_xO_{1-x} Al_xO_{1-x}, and Ga_xO_{1-x} as shown in Fig. 4a–c to validate our predictions. The convex hull in Fig. 4 is the outcome of Gibb's enthalpy analysis at a given temperature, which uses enthalpy of formation of different phases taking part in
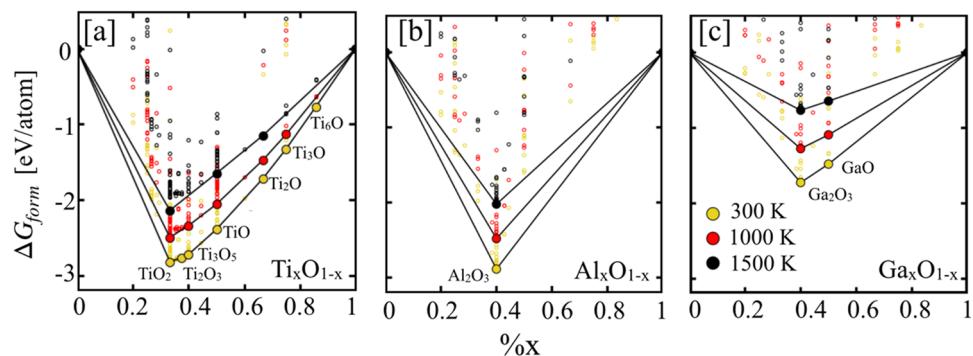
Figure 4. The temperature dependent convex hull of (**a**) Ti_xO_{1-x}, (**b**) Al_xO_{1-x}, and (**c**) Ga_xO_{1-x} shows the higher stability (Gibbs formation enthalpy) of key oxide phases TiO_2, Al_2O_3 and Ga_2O_3, which is in agreement with phases present NIST-JANAF thermochemical table[54,58].
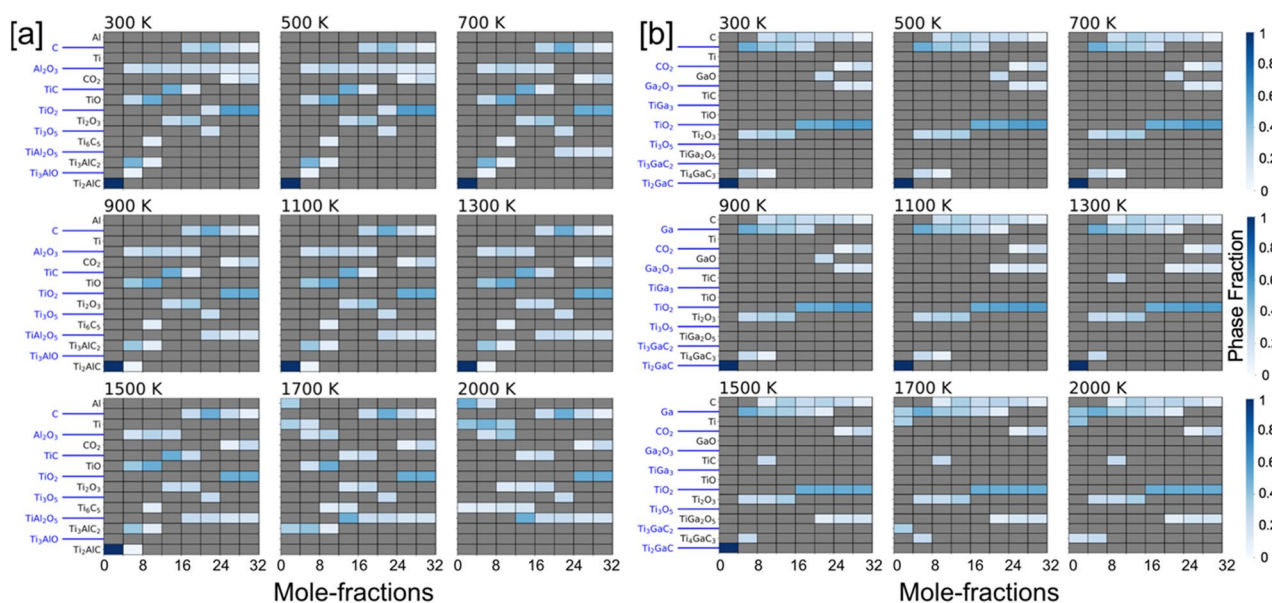

Figure 5. Phase fractions of (**a**) $[Ti_2AlC + O_2]$ and (**b**) $[Ti_2GaC + O_2]$ reaction products at different temperatures with increasing temperature from 300 to 2000 K with respect to molar percent oxygen (0–32 mol). The color gradient (shades of blue) shows molar phase fractions. Blank spot [gray (0)] suggests no phases.

equilibrium. The convex hull tells you that all phases on the hull compete successfully for equilibrium against other phases.
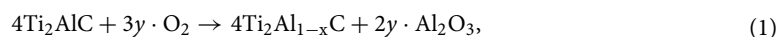
Our prediction of phase stability for Ti_xO_{1-x}, Al_xO_{1-x}, and Ga_xO_{1-x} based oxides was found in good agreement with experimental phases in NIST-JANAF thermochemical table[54,58]. Framework[52] predicts eight stable phases for Ti–O (TiO_2, Ti_2O_3, Ti_3O_5, TiO_3, TiO, Ti_2O, Ti_3O, and Ti_6O) in Fig. 4a, one for Al-–O (Al_2O_3) in Fig. 4b, and two phases in Ga–O (Ga_2O_3, GaO)[58] in Fig. 4c at 300 K. We show that Al_2O_3 and (GaO, Ga_2O_3) remains stable throughout the temperature range, while for Ti–O, two phases (Ti_2O; Ti_6O) disappear at 1500 K, which is in agreement with the phases reported in high-temperature thermochemical NIST-JANAF dataset[54]. Some of the phases of Ti_xO_{1-x} that undergo a phase change at higher temperatures are ignored[56]. The TiO_2, Al_2O_3 and Ga_2O_3 oxide phases that considered key for oxidation resistance remain most stable oxide phases, which may play a key role during oxidation process in disorder $Ti_2(Al_{1-x}Ga_x)C$ MAX phase. This is not straightforward conclusion as changing chemistries can have unexpected effects on phase formation and stability; therefore, it would be interesting to see how oxidizing environment impacts our final products and material survivability.

Oxidation analysis of $Ti_2(Al_{1-x}Ga_x)C$ MAX phases.

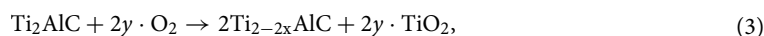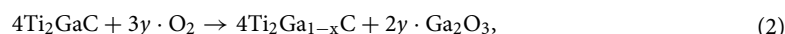(i) *x (Al) = 0.0 and 1.0* In Fig. 5a,b, we analyze the oxidation behavior of Ti_2AlC/Ti_2GaC and show the heat map of the molar phase-fractions of reaction products (the color bar on right represents the molar percent, or phase fraction, of each phase). In Fig. 5a, the heatmap shows the presence of Al_2O_3 at all temperatures

300–2000 K, whereas different Ti–O phases are observed at low (TiO), intermediate (TiO, Ti_2O_3, Ti_3O_5), and high (TiO_2) oxygen contents. At the onset of the oxidation process Al_2O_3, Ti_3AlC_2, and TiO forms first, which is followed by the reaction of oxygen with Ti_3AlC_2 that gradually transforms into TiC. At high oxygen contents, the MAX phase eventually disintegrates completely into solid Al_2O_3 and TiO_2, and gaseous CO_2 phase[52]. In Fig. 5a, the heat map for $Ti_2GaC + O_2$ shows the presence of Ga_2O_3 up to 1300 K. On the other hand, different Ti–O phases are observed similar to Ti_2AlC in Fig. 5a. At the onset of oxidation process and intermediate oxygen molar fractions Ga_2O_3 and GaO were observed. While higher order MAX phases such as Ti_3GaC_2, and Ti_4GaC_3 were found competing both at low and higher temperatures but at low oxygen content. The spinel type $TiGa_2O_3$ phase was observed at higher temperatures and high oxygen content. Both for Ti_2AlC and Ti_2GaC in Fig. 5a,b, the TiO forms first, which followed by the reaction of oxygen with higher order MAX phases gradually transforms to TiC. At high oxygen contents, the MAX phase eventually disintegrates completely into solid Al_2O_3, TiO_2, and gaseous CO_2 phase, which is in agreement with our oxide phase discussion in Figs. 3 and 4.
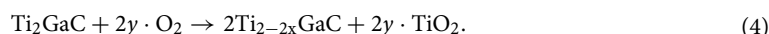
To understand the reaction mechanism arising changing chemical potential on varying molar oxygen percent, which represents the exposure time of the alloy to static air in experimental conditions. The reaction products of the chemical process during the selective oxidation of Al/Ga or Ti in Ti_2AlC/Ti_2GaC can be written as:

$$4Ti_2AlC + 3y \cdot O_2 \rightarrow 4Ti_2Al_{1-x}C + 2y \cdot Al_2O_3, \tag{1}$$

and

$$4Ti_2GaC + 3y \cdot O_2 \rightarrow 4Ti_2Ga_{1-x}C + 2y \cdot Ga_2O_3, \tag{2}$$

$$Ti_2AlC + 2y \cdot O_2 \rightarrow 2Ti_{2-2x}AlC + 2y \cdot TiO_2, \tag{3}$$

and

$$Ti_2GaC + 2y \cdot O_2 \rightarrow 2Ti_{2-2x}GaC + 2y \cdot TiO_2. \tag{4}$$

Considering longer exposure time to static air, C diffuses through TiO_2 and oxidizes into CO_2^-

$$Ti_2AlC + O_2 \rightarrow Al_2O_3 + TiO_2 + CO_2, \tag{5}$$

and

$$Ti_2GaC + O_2 \rightarrow Ga_2O_3 + TiO_2 + CO_2, \tag{6}$$

i.e., C from Ti-C diffuses through the mixed Ti-oxides layer and oxidize. The diffusion of Ti to the surface and O into the MAX phase or oxidation product during the oxidation process works as the rate-limiting condition.

Chemical activity of constituent elements of the [$Ti_2AlC/Ti_2GaC + O_2$]. The chemical activity of constituent elements of [$Ti_2AlC + O_2$] and [$Ti_2GaC + O_2$] during the oxidation process are shown in Fig. 6a,b. The (partial) chemical potential of (Ti, Al/Ga, C, O) is calculated for an open system using unknown molar concentration of reaction products by mixing of grand-canonical ΔG_{form} from 300 to 2000 K. The reaction chain is associated with the reductions in the partial chemical potentials of Ti and Al, but an increase in the chemical potential of O with increasing oxygen content while C remains almost unchanged except at high oxygen content and high temperature. The higher Ti/Al activity at the early oxidation stage is directly related to their partial chemical potentials. Two chemical potentials zones in Fig. 6a,b with increasing oxygen content are identified— (a) slowly varying (0–20 mol oxygen); and (b) sharp changing (> 20 mol oxygen). The sharp change in chemical potential occurs in the region > 10 mol oxygen as Ti_3AlC_2, Ti_3GaC_2, Ti_4GaC_3, Ti_3AlC_2, TiC completely disintegrates by then, moreover, C oxidizes to form gaseous CO_2. The occurrence of C and CO_2 at higher temperature suggests loss of carbon. The predicted trend in chemical potential suggests increased oxygen activity at higher oxygen content. It is obvious from Fig. 6a,b that Al activity is higher than Ga in MAX phase. This also could be correlated to Ellingham diagrams, where Al_2O_3 has much lower partial pressure compared to Ga_2O_3.

Elemental chemical potentials. Our framework treats all elemental reservoirs as an ideal gas model. The resulting phases at a particular temperature are determined by those that result in a minimal energy of the system. At any temperature the amount of oxygen is incrementally increased over a range of values, i.e., a variable oxygen reservoir. As more oxygen becomes available, greater oxygen dense phases are predicted to form Ti_2O over TiO_2. From a particular profile, we can solve for the individual chemical potentials using the GCLP model via relation $\mu_i = \partial U/\partial N$, where μ_i is the chemical potential of `i' element. The chemical potential of an oxygen gas molecule changes with temperature and partial pressure, however, we considered partial pressure of 1 atm in all our calculations assuming experimental conditions with normal pressure. The accepted energy of oxygen gas phase was calculated from DFT at (0 K), which is − 9.67 eV per atom, and listed in the OQMD dataset in the same manner as other unary components. The nominal change in oxygen ratio during oxidation reaction at each temperature changes the chemical potential when we solve grand canonical linear programming (GCLP) method. The temperature dependence of the chemical potential of oxygen is considered from the thermo-chemical tables[54].
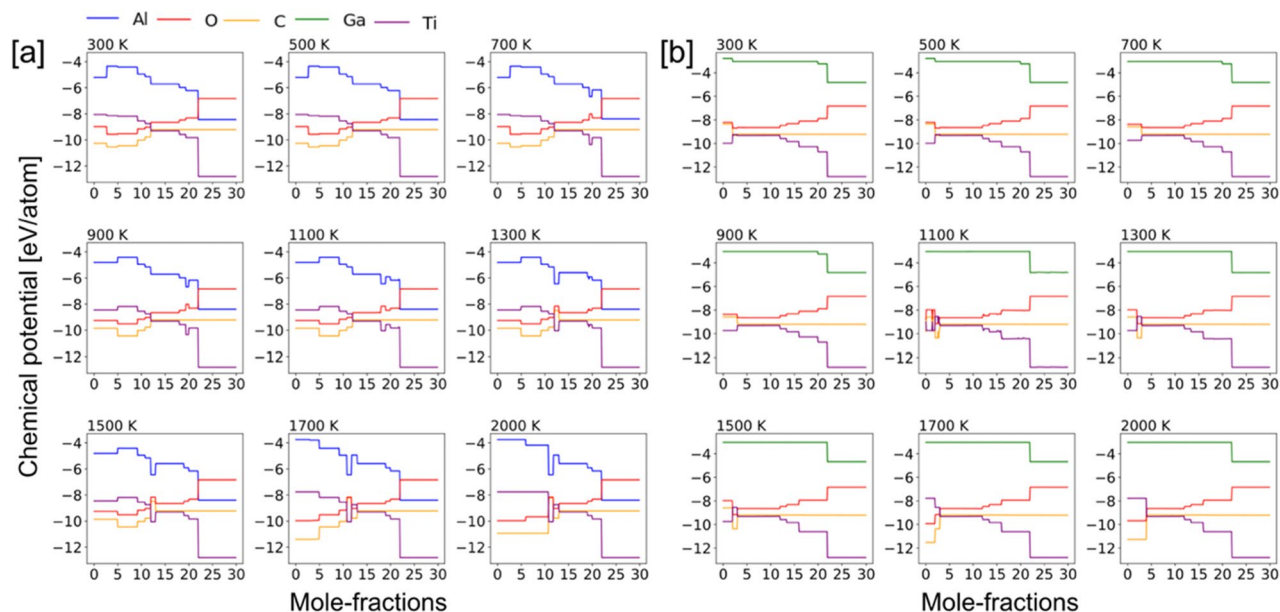
Figure 6. Oxidation reaction chain showing change in chemical potential of (**a**) [Ti$_2$AlC + O$_2$] and (**b**) [Ti$_2$GaC + O$_2$] as a function of changing molar percent oxygen from 300 to 1200 K. On oxidation, the partial chemical potentials of Ti/Al/Ga/C reduce while the chemical potential of invading O$_2$ increases.
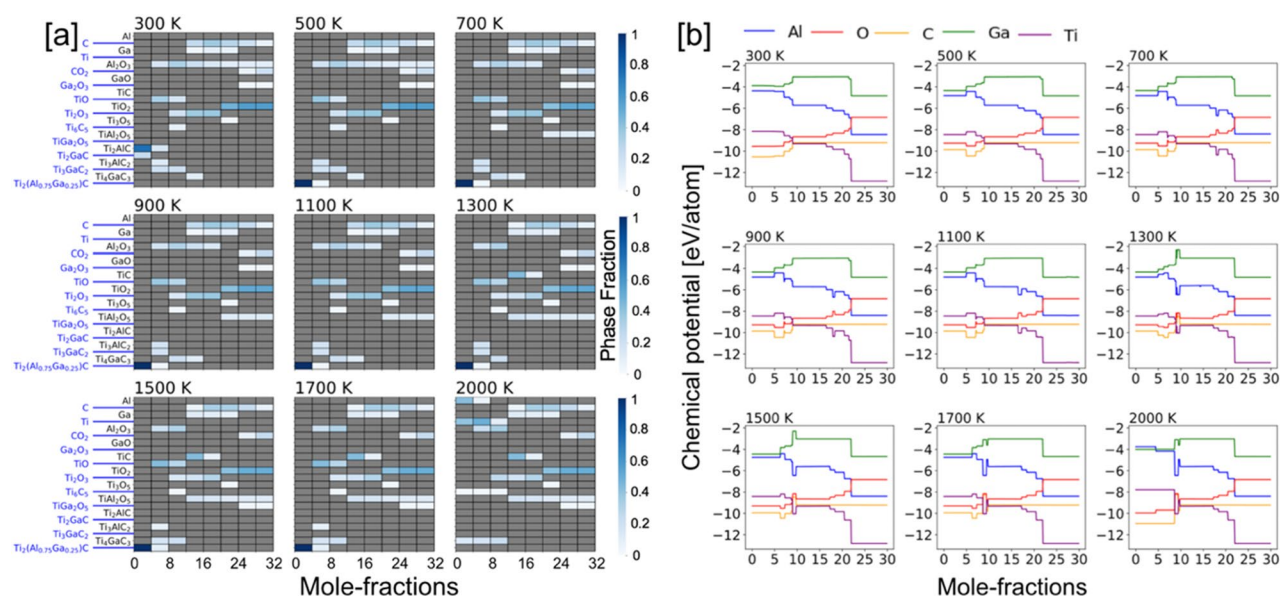

Figure 7. (**a**) Phase fractions and (**b**) chemical potential of [Ti$_2$(Al$_{0.75}$Ga$_{0.25}$)C + O$_2$] with increasing temperature from 300 to 2000 K and molar percent oxygen (0–32 mol). The color gradient (shades of blue) shows molar phase fractions. Blank spot [gray (0)] suggests no phases. On oxidation, the partial chemical potentials of Ti/Al/ Ga/C reduce while the chemical potential of invading O$_2$ increases.

(ii) *x (Al) = 0.75, 0.50, 0.25* We show the phase-fractions with increasing Ga at.% disorder at Al site of Ti$_2$AlC in Figs. 7, 8 and 9a, while respective chemical potentials are shown in Figs. 7, 8 and 9b. The heatmap of the molar phase-fractions of Ti$_2$(Al$_{0.75}$Ga$_{0.25}$)C + O$_2$ reaction product in Fig. 7a shows the presence of Al$_2$O$_3$ at all oxygen mole fractions and for 300–2000 K. On Ga alloying, a new Ti–O phase, Ti$_6$O$_{11}$, was observed at higher temperature and high oxygen. The oxidation reactions at low intermediate, and high oxygen exposure shows TiO, (TiO, Ti$_2$O$_3$, Ti$_3$O$_5$), and TiO$_2$ phases, respectively. We also predict the formation of a new complex oxide Ti–Ga–O phase, i.e., TiGa$_4$O$_8$. At the onset of oxidation process at higher temperature (> 700 K), the A-site disordered Ti$_2$(Al$_{0.75}$Ga$_{0.25}$)C MAX phase shows improved stability, which slowly transforms into Al$_2$O$_3$, Ti$_2$AlC, Ti$_2$GaC and TiO with increasing oxygen. Both Ti$_3$AlC$_2$ and Ti$_4$GaC$_3$ gradually transforms to TiC at higher temperature, and the MAX phase eventually disintegrates completely into solid Al$_2$O$_3$ and TiO$_2$, and gaseous CO$_2$ phase at high oxygen contents. We
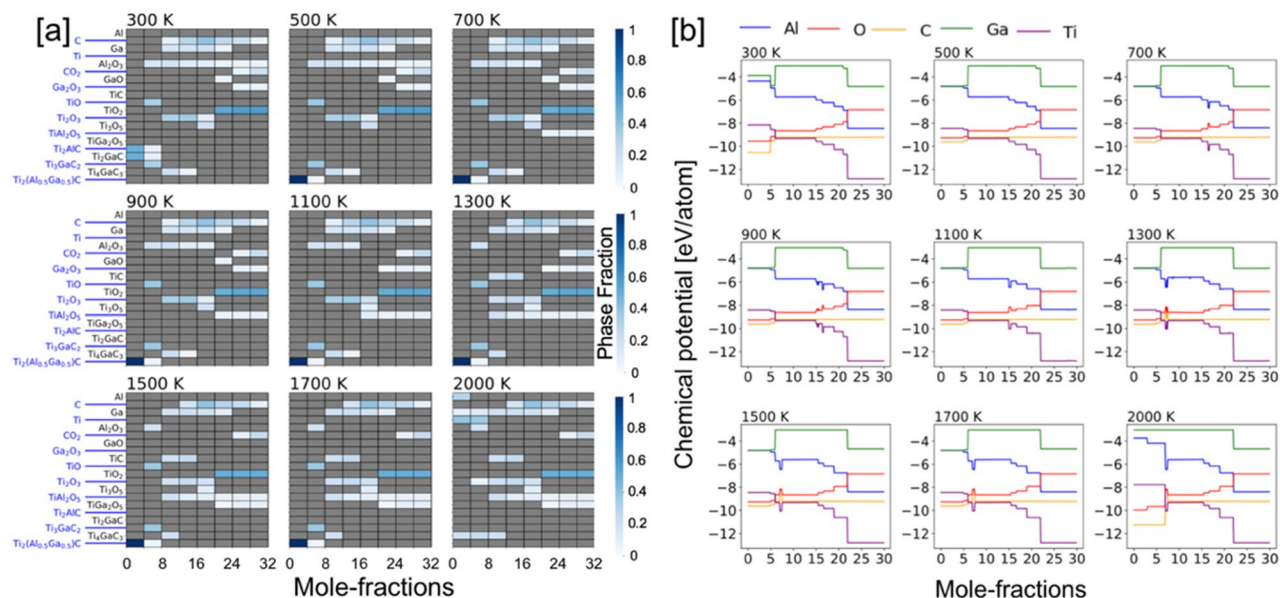
Figure 8. (**a**) Phase fractions and (**b**) chemical potential of $[Ti_2(Al_{0.50}Ga_{0.50})C+O_2]$ with increasing temperature from 300 to 2000 K and molar percent oxygen (0–32 mol). The color gradient (shades of blue) shows molar phase fractions. Blank spot [gray (0)] suggests no phases. Upon oxidation, the partial chemical potentials of Ti/Al/Ga/C reduce while the chemical potential of invading O_2 increases.
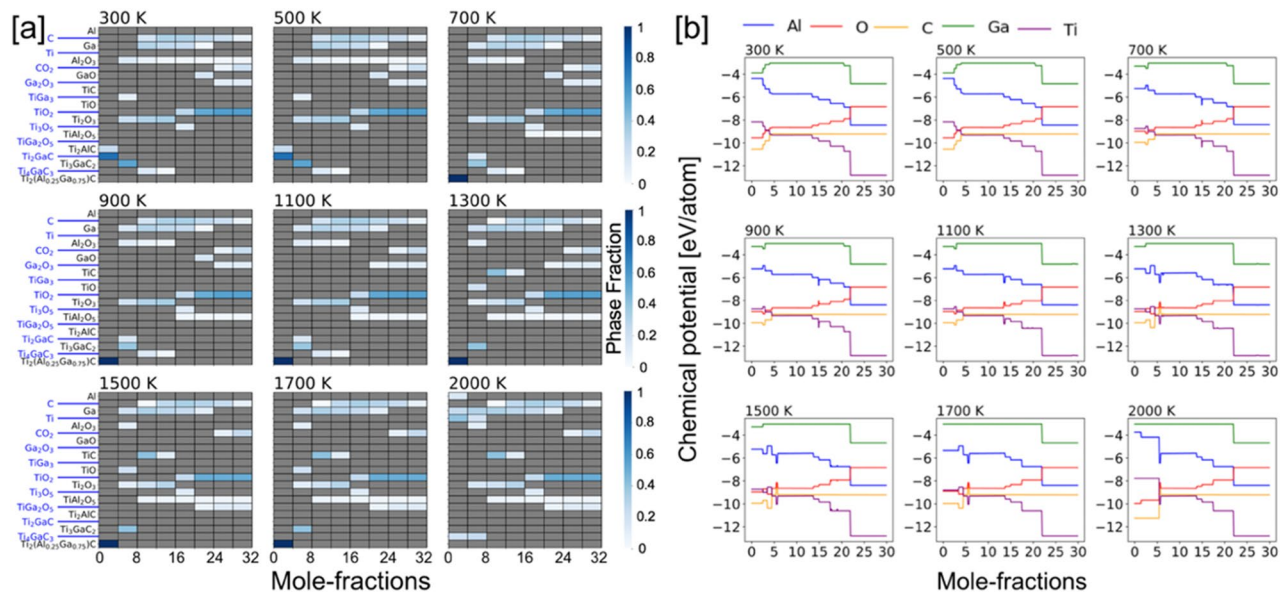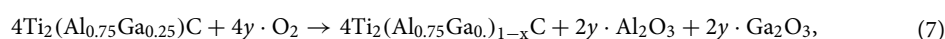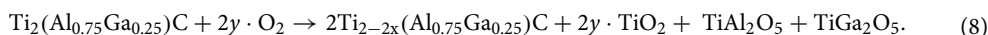

Figure 9. (**a**) Phase fractions and (**b**) chemical potential of $[Ti_2(Al_{0.25}Ga_{0.75})C+O_2]$ with increasing temperature from 300 to 2000 K and molar percent oxygen (0–32 mol). The color gradient (shades of blue) shows molar phase fractions. Blank spot [gray (0)] suggests no phases. On oxidation, the partial chemical potentials of Ti/Al/Ga/C reduce while the chemical potential of invading O_2 increases.

found a transient Ga based oxide Ga_2O_3 up to 1300 K at medium oxygen molar content and disappears at higher temperatures. The observations discussed were found true for all x(Ga) cases, i.e., x = 0.75, 0.50, 0.25 at.-frac. in Figs. 7, 8 and 9a.

We rewrote the Eqs. (1–3) which now include Ga Al-site, where we varied the molar oxygen percent and tracked the change chemical activity of elements as shown in Figs. 7, 8 and 9b, which represents the exposure time of the alloy to static air in experimental conditions. The reaction products of the chemical process during the selective oxidation of Al/Ga or Ti in $Ti_2(Al_{0.75}Ga_{0.25})C$ can be written as:

$$4Ti_2(Al_{0.75}Ga_{0.25})C + 4y \cdot O_2 \rightarrow 4Ti_2(Al_{0.75}Ga_{0.})_{1-x}C + 2y \cdot Al_2O_3 + 2y \cdot Ga_2O_3, \quad (7)$$

and

$$Ti_2(Al_{0.75}Ga_{0.25})C + 2y \cdot O_2 \rightarrow 2Ti_{2-2x}(Al_{0.75}Ga_{0.25})C + 2y \cdot TiO_2 + TiAl_2O_5 + TiGa_2O_5. \quad (8)$$

Considering longer exposure time to static air, C diffuses through TiO_2 and oxidizes into CO_2 while we also observe that the Ga based intermetallic phase shows very high stability.

$$Ti_2(Al_{0.75}Ga_{0.25})C + O_2 \rightarrow Al_2O_3 + TiO_2 + GaO + Ga_2O_3 + CO_2. \quad (9)$$
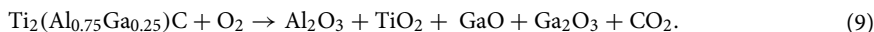
Chemical activity of Ti/Al/Ga/C in $Ti_2(Al_{1-x}Ga_x)C$. The chemical activity of the constituent elements in $[Ti_2(Al_{1-x}Ga_x)C + O_2]$ during the oxidation process are shown in Figs. 7, 8 and 9b. The (partial) chemical potential of (Ti, Al/Ga, C, O) is shown from 300 to 2000 K and is calculated by the mixing of ΔG_{form} using GCLP. Similar to Ti_2AlC, the reaction chain associated with the reductions in the partial chemical potentials of Ti and Al is shown. The chemical potential of Ga slightly increases then decreases, possibly due to the appearance of metastable oxide phase GaO, which disappears at higher temperature and high oxygen content. The increase in the O chemical potential with increasing oxygen content while C remains almost unchanged or weakly changed except at high oxygen content and high temperature. The higher Ti/Al activity compared to Ga at the early oxidation stage is directly related to their partial elemental chemical potentials. Two chemical potentials zones in Figs. 7, 8 and 9b with increasing oxygen content are identified—(a) slowly varying (0–10 mol oxygen); and (b) sharp changing (> 10 mol oxygen). The sharp change in chemical potential occurs in the region > 10 mol oxygen as $Ti_2AlC_2/Ti_3AlC_2/TiC$ completely disintegrates by then, moreover, C oxidizes to form gaseous CO_2. The occurrence of C and CO_2 at higher temperature suggests loss of carbon. The predicted trend in chemical potential suggests increased oxygen activity at higher oxygen content. Similarly, for Ga doped cases, we observed that chemical activity of Al increased in the intermediate and higher exposure to oxygen at all temperatures compared to pure Ti_2AlC in Fig. 6. This suggests that Ga can be used as a catalyst in Al based MAX phases to control the elemental chemical activity.

Discussion

The Al_2O_3 was seen at all temperatures and all oxygen concentrations due to the high chemical activity of Al, see Figs. 5, 7, 8 and 9a, as well as the very exothermic nature of the Al_2O_3 phase itself. The weak metallic bonding between Ti–Al (2.84 Å) compared to Ti–Ga (2.79 Å) also contribute to the increased Al diffusivity[60], which results into later appearance of Ga-based phases at low temperature and low oxygen content. The formation of Al_2O_3 results into Al/Ga depletion in $Ti_2(Al_{1-x}Ga_x)C$ at the early-stage oxidation. This in turn leads to the decomposition of the MAX phases into TiO, Al_2O_3, and Ti_2AlC/Ti_2GaC, Ti_3AlC_2 and Ti_4GaC_3 at low oxygen concentration. This indicates that Ti and Al/Ga are the first oxidizing elements when $Ti_2(Al_{1-x}Ga_x)C$ in Figs. 7, 8 and 9 was exposed to ambient air at elevated temperatures. On further increasing the oxygen concentrations, the Al_2O_3 oxide scale remains stable compared to other oxides as partial pressure to form Al_2O_3 is much lower than of TiO_2[61] or Ga based phases[62]. The weaker binding of Al with C or Ti[63,64] in $Ti_2(Al_{1-x}Ga_x)C$ compared to Ga and better Al diffusion[60] eases the Al_2O_3 growth. The better thermodynamic stability of Al_2O_3 compared to other phases during oxidation of Ti–Al–Ga–C also helps in stabilizing Al_2O_3 at elevated temperatures. The C and CO_2 appear as the reaction products at higher temperature, which suggests C loss and the evaporation of CO_2 from the oxide scale[62]. The reaction product of in $Ti_2(Al_{1-x}Ga_x)C$ oxidation reaction correctly reproduces experimentally observed phase-fractions. We also found that Al_2O_3 forms at all temperature and all oxygen contents but Al_2O_3 stops forming at very high-T and high-O_2 due to higher stability of spinel phase oxides. The appearance of a more stable spinel oxide phase hampers the Al_2O_3 formation, which is the reason Al_2O_3 is not observed at high-T. For clarity, however, the Al_2O_3 formed at the early oxidation stage will remain in the system and work as a protective layer. Notably, the spinal phase becomes more favorable both due to its favorable thermodynamics and requirement of low Al content.

Electronic-structure of $Ti_2(Al_{1-x}Ga_x)C$ MAX. As discussed in the oxidation section, the chemical activity of Al has increased as the Ga reduces the interaction with M–A layer. The question arises that what changes in the electronic structure correlates with the oxidation behavior in the MAX phase. The detailed electronic nature of $Ti_2(Al_{1-x}Ga_x)C$ was analyzed using electronic density of states (DOS) and charge-density difference in Figs. 10 and 11, respectively.

The DOS is an effective tool to reveal the hybridization among the different electronic states. In Fig. 10a–d, we plot total and partial DOS to understand the effect of Ga alloying, where the Fermi level (E_{Fermi}) is set at zero. Our goal is to understand to role of electronic structure on oxidation behavior of $Ti_2(Al_{1-x}Ga_x)C$ MAX. The Ga doping in Fig. 10a shows strong change Ti-3d and Ga-4p states near − 4 eV and − 1 eV as shown in two highlighted zones. Clearly, the DOS in Ga doped cases is significantly reduced compared to parent phase, i.e., Ti_2AlC MAX. The prime contribution at the E_F in the DOS comes from the Ti-3d ([Ar]3$d^2$4s^2) states as shown in Fig. 10b–d, while Ga-4p ([Ar]4$s^2$4p^1) and Al-3p ([Ne]3$s^2$3p^1) also contribute but lesser in magnitude compared to the Ti-3d. The valence states could be divided into three energy range, i.e., (i) − 12.0 eV to − 9.0 eV, (ii) − 9.0 eV to − 2.0 eV, and (iii) − 2.0 to 0.0. The DOS at the lower energies in the region (i) show peaks at nearly − 10 eV is mainly comprised of Ti-3d and C-2s below the E_F (not shown in the Fig. 10 as they are not chemically activity), which gives rise to the formation of stronger Ti–C bonds. While energy states for Ga doped cases in the region (ii) comprised of Ti-3d, Al-3p, and Ga-4p in Fig. 10b–d. Notably, in the region (iii), we found an increased Ga-4p states near the E_F, which shows strong overlap with Ti-3d bands.

The DOS in both parent and Ga-doped phases are mainly contributed by the Ti-3d^2, C-2p^1, and Al-3p^1 states. The Ti-3d and Ga-4p/Al-3p hybridized strongly that lead the peaks in the low energy region of both total and
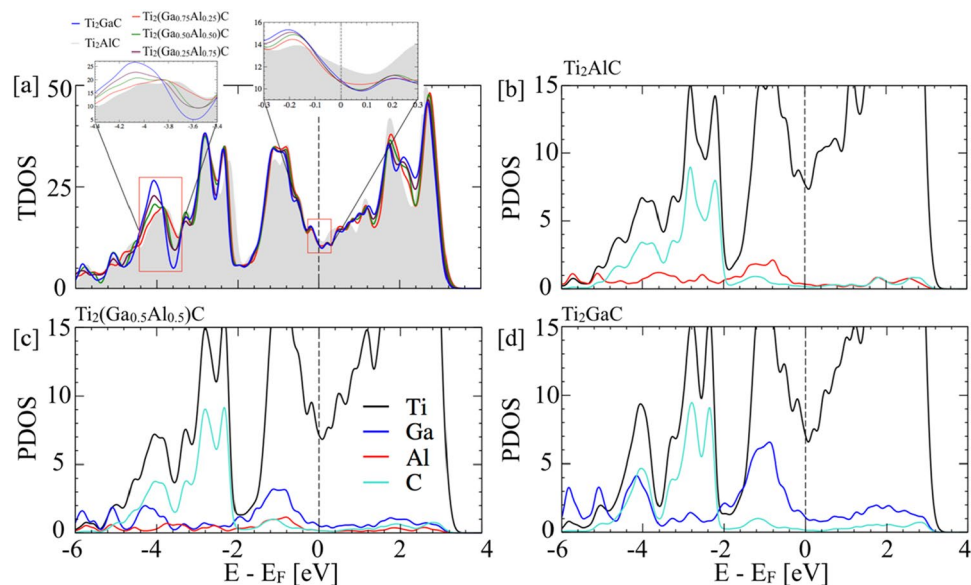
Figure 10. (**a**) The total density of states (DOS) with A-site disorder by Ga in Ti_2AlC MAX. (**c,d**) The partial DOS of $Ti_2(Al_{1-x}Ga_x)C$ for x = 0, 0.50, and 1. The crystal orbital Hamilton population (COHP) analysis for Ti_2AlC and Ti_2GaC is provided later in bond analysis section.
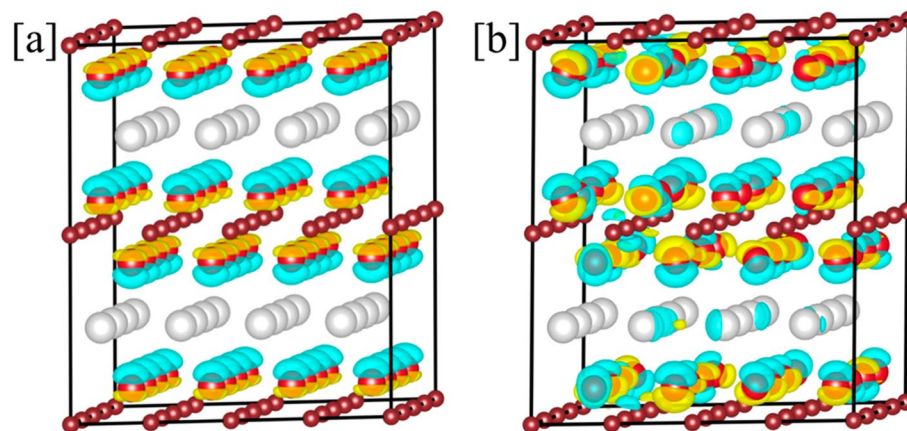

Figure 11. The charge density difference ($\Delta\rho$) for (**a**) ρ (x = 1.0)–ρ (x = 0), and (**b**) ρ (x = 1.0)–ρ (x = 0.50) in $Ti_2(Al_{1-x}Ga_x)C$ MAX with respect to Ti_2AlC, x is represented in atomic fractions.

partial DOS. The energy region of 0 to − 6 eV is dominated by Ti-3d which is also hybridized with the Ga-4p/Al-2p. The peaks in the DOS in Fig. 10 are the consequence of the hybridization between different orbitals that defines the energy of the hybridized states. The peak positions show weak shift both in the valence and the conduction bands, which is expected to have no major effects on electronic structure. Meanwhile, the partial DOS analysis in Fig. 10b–d, shows changes in hybridization between Ti and C when Al is doped with Ga, while the MAX phase remains thermodynamically stable in the hexagonal phase. This change in energy of bonding states due to Ga-doping reflects the change in the Ti–C hybridization strength, consequently, the bonding strength between unlike atoms. The finite DOS at the E_F indicates that doped Ga atoms could not change the metallic character. At the top of the valence band, an interaction between Ti-3d and C-2p peaks in the energy range of − 2.0 eV and − 5 eV that leads to strong hybridization, and results into a strong directional bonding.

A peak or a valley like structure in DOS at E_F signifies the presence of a pseudo gap, which is a signature of both chemical and structural stability[59,65–67]. The presence of pseudo-gap region and alloys stability has its origin in several active electronic mechanisms including charge transfer and change in hybridization that pulls down the electronic DOS from E_F either below the Fermi level or above it[67,68]. In Fig. 10, we found that the decreases electronic density of states at E_F originates from change in mixing of the Ti-3d states with Al-3p due to Ga alloying, which shows increase in Ga-4p states near − 1 eV with increasing at.% Ga. This correlates well with the
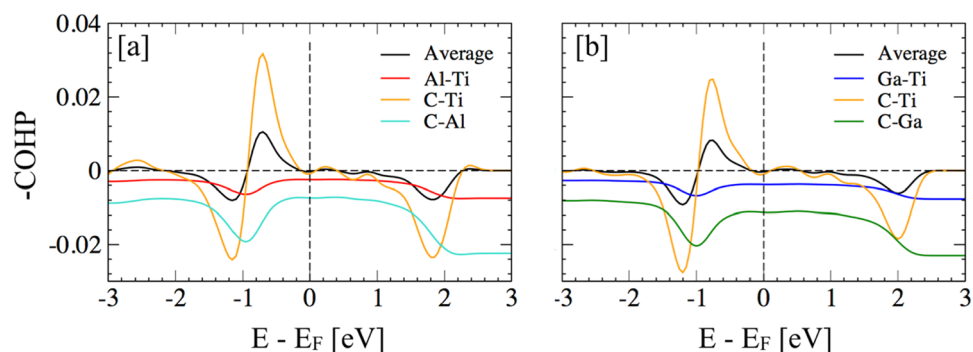
Figure 12. The crystal orbital Hamilton population (COHP) analysis was done for three short Al/Ga–Ti, C–Ti, C–Al/Ga bonds in Ti$_2$AlC and Ti$_2$GaC MAX. The energies are shown relative to the Fermi level.

stability analysis in Figs. 1 and 2 (see Table 1). The A-site alloying weakens the bonding in Ti–Al–Ga–C MAX. This suggests that Ga can be tuned to manipulate chemical activity of Al based MAX.

The charge density analysis:

The direction of intra-layer (Ti–C/Al–Ga) and inter-layer (Al/Ga–C) charge transfer is also an important feature of MAX phase stability. In Fig. 11a,b, we plot the charge density difference ($\Delta\rho = \rho_{Ti2(Al1-Gax)C} - \rho_{Ti2AlC}$) for Ti$_2$(Al$_{1-}Ga_x$)C for x = 1.0, and 0.50, where blue color represents the charge from the Ti$_2$AlC MAX while the yellow color is charge readjustment. Our charge plot in Fig. 11 shows no effective change in charge at C and Ti loses the charge. This charge asymmetry at site A-site was caused by Ga alloying in the Ti$_2$AlC MAX, therefore, a varying strength of Al/Ga metallic bonds are expected. The effective charge transfer between Ga to Al shows the mechanism controlling the bonding behavior in MAX phase, which also weakens the bonding Al interaction with the Ti–C basal plane. This gain in charge density in Ti$_2$GaC originates from decrease of 1.4% volume with respect to Ti$_2$AlC, which is possibly one of the reasons why Al chemical activity has increased with Ga doping.

Chemical bonding analysis. We performed crystal orbital Hamilton population (COHP) analysis to elucidate the bonding behavior[69–73]. The COHP partitions the band structure energy into bonding, nonbonding and antibonding energy of atomic pair contribution in a specified energy range. In Fig. 12a,b, we plot-pCOHP as a function of energy for Ti$_2$(Al$_{1-x}$Ga$_x$)C, x = 0,1. Positive values of –pCOHP describe bonding energy regions whereas negative values describe antibonding energy regions. The COHP shows slightly different picture of bonding for Ti$_2$GaC MAX in Fig. 12b, where Ga shows weak reduction of C-Ti bonding strength while weak increase in anti-bonding states. This indicates towards increased charge activity due to Ga as shown by charge density difference plot in Fig. 10. Notably, the antibonding states for the C–Ti appear near − 1.2 eV below the Fermi level both for Ti$_2$AlC (− 1.17 eV in Fig. 12a) and Ti$_2$GaC (− 1.2 eV in Fig. 12b). Both bonding and antibonding states in Ti$_2$GaC show a shift below Fermi level due to charge filling, which again corroborate with our idea of increase charge activity. This is also in agreement with the fact that the Ga doping leads to lower volume and lower enthalpy as shown in Tables 1 and 2. Expectedly, Ga/Al–Ti or Ga/Al–C show antibonding (negative COHP) in the whole energy range as Al/Ga and Ti–C are in two different basal planes in MAX phase.

Conclusion

We systematically investigated the thermodynamic stability and oxidation behavior of Ti$_2$AlC MAX phases with Ga alloying using high-throughput machine-learning framework combined with density-functional theory. The A-site (at Al) disordering of Ti$_2$AlC with Ga shows significant change in the chemical activity of Al with increasing temperature and exposure to static oxygen. Our thermodynamic analysis shows changes in the ΔG_{form} at higher temperatures, which implies an interplay of temperature-dependent enthalpy and entropic contributions in oxidation behavior of Ga doped Ti$_2$AlC MAX phase. Therefore, we have included electronic, chemical, and vibrational entropy contribution with vibrational contribution is the largest and has significant impact on high-temperature stability of MAX phases. Our convex hull analysis of key Ti–O, Al–O, and Ga–O oxides provides validation of our framework that provides accurate phase predictions, which is critical in oxidation analysis. We also show that the increased Al activity during oxidation in Ga doped MAX phases may improve the oxide layer (Al$_2$O$_3$) formation, which will serve as protection against oxygen diffusion by delaying the formation Ti–O (e.g., TiO$_2$) based phases. This also suggests that Al at.% in bulk Ti$_2$(Ga$_x$Al$_{1-x}$)C MAX is sufficient, which also indicates that improved Al activity can be significant in enhancing the protection of MAX phases against oxidation.

The phase stability analysis is an efficient determination of the most stable equilibrium state that helps to assess the resulting reaction products for a given set of reactants. We performed detailed electronic-structure, charge density, and chemical bonding (COHP) analysis to understand the change in oxidation behavior of of Ga doped Ti$_2$AlC, i.e., Ti$_2$(Ga$_x$Al$_{1-x}$)C MAX. Expectedly, the COHP analysis shows that covalently bonded Ti-C shows the bonding nature in (0001) basal plane compared other pairs such as Ti–Al/Ga or C–Al/Ga, which is clearly observed by their anti-bonding behavior. The anti-bonding of Ti–Al and Ti–Ga bonds makes them easier to break, however, stronger stability of Ga doped MAX phases weakens the chemical bonding of Al with Al–Ga layer. This makes the chemical activity of Al higher compared to Ga[74], therefore, Al atoms can diffuse easily and

are readily available to form a high density protective Al_2O_3 layers, i.e., inward oxygen flow can be slowed down and improve the oxidation resistance of MAX phases. The electronic-structure analysis shows change in inter-layer interaction between Ti–C and Al/Ga as one of the reasons why Al chemical activity may increase with Ga doping. This study can be useful guideline to understand to role of alloying on electronic, thermodynamic, and oxidation related mechanisms in other MAX phases. Since the oxidation is a surface phenomenon, our study may also be helpful to understand the oxidation behavior of two-dimensional (2D) MAX phases, i.e., MXenes (transition metal carbides, carbonitrides and nitrides).

Data availability

The data used in the manuscript is available with corresponding author on reasonable request.

References

1. Barsoum, M. W. The $M_{N+1}AX_N$ phases: A new class of solids: Thermodynamically stable nanolaminates. *Prog. Solid State Chem.* **28**, 201 (2000).
2. Music, D. & Schneider, J. M. The correlation between the electronic structure and elastic properties of nanolaminates. *JOM* **59**, 60 (2007).
3. Eklund, P., Beckers, M., Jansson, U., Högberg, H. & Hultman, L. The $M_{n+1}AX_n$ phases: Materials science and thin-film processing. *Thin Solid Films* **518**, 1851 (2010).
4. Barsoum, M. W. & Radovic, M. Elastic and mechanical properties of the MAX phases. *Ann. Rev. Mater. Res.* **41**, 195 (2011).
5. Wang, J. Y. & Zhou, Y. C. Recent progress in theoretical prediction, preparation, and characterization of layered ternary transition-metal carbides. *Ann. Rev. Mater. Res.* **39**, 415 (2009).
6. Tallman, D. J., Anasori, B. & Barsoum, M. W. A critical review of the oxidation of Ti_2AlC, Ti_3AlC_2 and Cr_2AlC in air. *Mater. Res. Lett.* **1**, 115–125 (2013).
7. Prescott, R. & Graham, M. J. The formation of aluminum oxide scales on high-temperature alloys. *Oxid. Met.* **38**, 233–254 (1992).
8. Barsoum, M. W., Ho-Duc, L. H., Radovic, M. & El-Raghy, T. Long time oxidation study of Ti_3SiC_2, Ti_3SiC_2/SiC, and Ti_3SiC_2/TiC composites in air. *J. Electrochem. Soc.* **150**, B166–B175 (2003).
9. Wang, J. & Zhou, Y. Recent progress in theoretical prediction, preparation, and characterization of layered ternary transition-metal carbides. *Annu. Rev. Mater. Res.* **39**, 415–443 (2009).
10. Cui, B. & Lee, W. E. High-temperature oxidation behaviour of MAX phase ceramics. *Refractories Worldforum* **5**, 105–112 (2013).
11. Lee, W. E., Zhang, S. & Karakus, M. Refractories: Controlled microstructure composites for extreme environments. *J. Mater. Sci.* **39**, 6675–6685 (2004).
12. Cui, B., Jayaseelan, D. D. & Lee, W. E. Microstructural evolution during high-temperature oxidation of Ti_2AlC ceramics. *Acta Mater.* **59**, 4116–4125 (2011).
13. Cui, B., Jayaseelan, D. D. & Lee, W. E. TEM study of the early stages of Ti_2AlC oxidation at 900 °C. *Scr. Mater.* **67**, 830–833 (2012).
14. Weber, W. J., Wang, L. M. & Yu, N. The irradiation-induced crystalline-to-amorphous phase transition in α-SiC. *Nucl. Instrum. Method B* **116**, 322 (1996).
15. Nappé, J. C. *et al.* Structural changes induced by heavy ion irradiation in titanium silicon carbide. *J. Nucl. Mater.* **409**, 53 (2011).
16. Buchholt, K. *et al.* Ohmic contact properties of magnetron sputtered Ti_3SiC_2 Ti_3SiC_2 on n- and p type 4H-silicon carbide. *Appl. Phys. Lett.* **98**, 042108 (2011).
17. Wang, Z. C., Saito, M., Tsukimoto, S. & Ikuara, Y. Interface atomic-scale structure and its impact on quantum transport. *Adv. Mater.* **21**, 4966 (2009).
18. Sokol, M., Yang, J., Keshavan, H. & Barsoum, M. W. Bonding and oxidation protection of Ti_2AlC and Cr_2AlC for a Ni-based superalloy. *J. Eur. Ceram. Soc.* **39**, 878–882 (2019).
19. Bouhemadou, A. & Khenata, R. Prediction study of structural and elastic properties under the pressure effect of M_2GaC (M = Ti, V, Nb, Ta). *J. Appl. Phys.* **102**, 043528 (2007).
20. Music, D., Ahuja, R. & Schneider, J. M. Surface energy of M2AC(0001) determined by density functional theory (M = Ti, V, Cr; A = Al, Ga, Ge). *Surf. Sci.* **601**, 896 (2007).
21. Hug, G. Electronic structures of and composition gaps among the ternary carbides Ti_2MC. *Phys. Rev. B* **74**, 184113 (2006).
22. Mo, Y., Rulis, P. & Ching, W. Y. Electronic structure and optical conductivities of 20 MAX-phase compounds. *Phys. Rev. B* **86**, 165122 (2012).
23. Duong, T., Gibbons, S., Kinra, R. & Arróyave, R. Ab-initio aprroach to the electronic, structural, elastic, and finite-temperature thermodynamic properties of Ti2AX (A = Al or Ga and X = C or N). *J. Appl. Phys.* **110**, 093504 (2011).
24. Iwaszuk, A., Mulheran, P. A. & Nolan, M. TiO_2 nanocluster modified-rutile TiO_2 photocatalyst: A first principles investigation. *J. Mater. Chem. A* **1**, 2515 (2013).
25. Akimov, A. I., Tkachenko, T. M. & Lebedev, S. A. Thallium-based high-temperature 2212 superconductor with partial substitution of oxygen by fluorine and of calcium by cerium. *Inorg. Mater.* **42**, 331 (2006).
26. Li, X., Xie, X., Gonzalez-Julian, J., Malzbender, J. & Yang, R. Mechanical and oxidation behavior of textured Ti_2AlC and Ti_3AlC_2 MAX phase materials. *J. Eur. Ceram. Soc.* **40**(15), 5258–5271 (2020).
27. Gu, J. *et al.* Mechanical properties and oxidation behavior of Ti-doped Nb_4AlC_3. *J. Eur. Ceram. Soc.* **36**, 1001–1008 (2016).
28. Wang, J., Wang, J., Zhou, Y. & Hu, C. Phase stability, electronic structure and mechanical properties of ternary-layered carbide Nb4AlC3: An ab initio study. *Acta Mater.* **56**, 1511–1518 (2008).
29. Nie, J., Liu, S., Zhan, X., Ao, L. & Li, L. First-principles study of Hf/Nb/Zr- doped MAX phases Ti_3AlC_2 and Ti_3SiC_2. *Phys. B* **571**, 105–111 (2019).
30. Hadi, M. A. *et al.* Phase stability and physical properties of $(Zr_{1-x}Nb_x)_2AlC$ MAX phases. *J. Phys. Chem. Solids* **132**, 38–47 (2019).
31. Hadi, M. A. *et al.* Effects of Al substitution by Si in Ti_3AlC_2 nanolaminate. *Sci. Rep.* **11**, 3410 (2021).
32. Hadi, M. A. *et al.* Insights into the physical properties of a new 211 MAX phase Nb_2CuC. *J. Phys. Chem. Solids* **149**, 109759 (2021).
33. Ghebouli, B. *et al.* Structural, elastic and electronic properties for M2XC (M = Ti and Cr, X = Ga and Al) phases from ab initio calculations. *Acta Metall. Sin.* **24**(4), 255 (2011).
34. Nordlund, K., Keinonen, J., Ghaly, M. & Averback, R. S. Coherent displacement of atoms during ion irradiation. *Nature* **398**, 49–51 (1999).
35. Zhang, Y. *et al.* Ionization-induced annealing of pre-existing defects in silicon carbide. *Nat. Commun.* **6**, 8049 (2015).
36. Zhang, Y. *et al.* Influence of chemical disorder on energy dissipation and defect evolution in concentrated solid solution alloys. *Nat. Commun.* **6**, 8736 (2015).
37. Was, G. S., Averback, R. S., & Konings, R. J. M. (ed.) *Comprehensive Nuclear Materials*, vol. 1 293–332 (Elsevier Ltd, 2012).
38. Kresse, G. & Furthmüller, J. Efficient iterative schemes for ab initio total-energy calculations. *Phys. Rev. B* **54**, 11169–11186 (1996).

39. Kresse, G. & Hafner, J. Ab initio molecular dynamics for liquid metals. *Phys. Rev. B* **47**, 558–561 (1993).
40. Kresse, G. & Furthmüller, J. Efficiency of ab-initio total energy calculations for metals and semiconductors using a plane-wave basis set. *Comput. Mater. Sci.* **6**, 15–50 (1996).
41. Perdew, J. P., Burke, K. & Ernzerhof, M. Generalized gradient approximation made simple. *Phys. Rev. Lett.* **77**, 3865–3868 (1996).
42. Monkhorst, H. J. & Pack, J. D. Special points for Brillouin-zone integrations. *Phys. Rev. B* **13**, 5188 (1976).
43. Kresse, G. & Joubert, D. From ultrasoft pseudopotentials to the projector augmented-wave method. *Phys. Rev. B* **59**, 1758–1775 (1999).
44. Blöchl, P. E. Projector augmented-wave method. *Phys. Rev. B* **50**, 17953–17979 (1994).
45. Söderlind, P., Turchi, P. E. A., Landa, A. & Lordi, V. Ground-state properties of rareearth metals: An evaluation of density-functional theory. *J. Phys.* **26**, 416001 (2014).
46. Giese, T. J. & York, D. M. A GPU-accelerated parameter interpolation thermodynamic integration free energy method. *J. Chem. Theory Comput.* **14**, 1564–1582 (2018).
47. Singh, P., Harbola, M. K., Sanyal, B. & Mookerjee, A. Accurate determination of band gaps within density functional formalism. *Phys. Rev. B* **87**, 235110 (2013).
48. Singh, P., Harbola, M. K., Hemanadhan, M., Mookerjee, A. & Johnson, D. D. Better band gaps with asymptotically corrected local exchange potentials. *Phys. Rev. B* **93**, 085204 (2016).
49. Roy, A. *et al.* Vacancy formation energies and migration barriers in multi-principal element alloys. *Acta Mater.* **226**, 117611 (2022).
50. Ouyang, R., Curtarolo, S., Ahmetcik, E., Scheffler, M. & Ghiringhelli, L. M. SISSO: A compressed-sensing method for identifying the best low-dimensional descriptor in an immensity of offered candidates. *Phys Rev. Mater.* **2**(8), 083802 (2018).
51. Akbarzadeh, A. R., Ozolins, V. & Wolverton, C. First-principles determination of multicomponent hydride phase diagrams: Application to the Li–Mg–N–H system. *Adv. Mater.* **19**, 3233–3239 (2007).
52. Sauceda, D. *et al.* High-throughput reaction engineering to assess the oxidation stability of MAX phases. *NPJ Comput. Mater.* **7**, 6 (2021).
53. Singh, P., Sauceda, D. & Arroyave, R. High temperature oxidation behavior of disordered (Ti$_{0.5}$Zr$_{0.5}$)2AlC MAX phase via a Machine Learning-Augmented DFT approach. *Mater. Lett. X* **10**, 100062 (2021).
54. Chase, M. W. Jr. *et al.* JANAF thermochemcial table 3d edition. *J. Phys. Chem. Ref. Data.* **14**, 2 (1985).
55. Saal, J. E., Kirklin, S., Aykol, M., Meredig, B. & Wolverton, C. Materials design and discovery with high-throughput density functional theory: The open quantum materials database (OQMD). *JOM* **65**, 1501–1509 (2013).
56. Bartel, C. J. *et al.* Physical descriptor for the Gibbs energy of inorganic crystalline solids and temperature-dependent materials chemistry. *Nat. Commun.* **9**, 4168 (2018).
57. Zinkevich, M. & Aldinger, F. Thermodynamic assessment of the gallium-oxygen system. *J. Am. Ceram. Soc.* **87**, 683–691 (2004).
58. Jain, A. *et al.* Commentary: The Materials Project: A materials genome approach to accelerating materials innovation. *APL Mater.* **1**, 011002 (2013).
59. Villarreal, R., Singh, P. & Arroyave, R. Metric-driven search for structurally stable inorganic compounds. *Acta Mater.* **202**, 437–447 (2021).
60. Singh, P., Sauceda, D. & Arroyave, R. The effect of chemical disorder on defect formation and migration in disordered MAX phases. *Acta Mater.* **184**, 50–58 (2019).
61. Bandyopadhyay, D. The Ti–Si–C system (Titanium–Silicon–Carbon). *J. Phase Equilib. Diffus.* **25**, 415 (2004).
62. Kesmeyanov, A. K. *Vapour Pressure of the Elements, Translated and edited by J. 1. Cal'asso* (Academic Press, 1963)
63. Liao, T., Wang, J. & Zou, Y. Ab initio modeling of the formation and migration of monovacancies in Ti$_2$AlC. *Scr. Mater.* **59**, 854–857 (2008).
64. Du, Y. *et al.* Anisotropic corrosion of Ti$_2$AlC and Ti$_3$AlC$_2$ in supercritical water at 500 °C. *Ceram. Int.* **43**, 7166–7171 (2017).
65. Basu, S., Obando, N., Gowdy, A., Karaman, I. & Radovic, M. Long-term oxidation of Ti$_2$AlC in air and water vapor at 1000–1300°C temperature range. *J. Electrochem. Soc.* **159**, C90 (2011).
66. Singh, P., Smirnov, A. V. & Johnson, D. D. Ta–Nb–Mo–W refractory high-entropy alloys: Anomalous ordering behavior and its intriguing electronic origin. *Phys. Rev. Mater.* **2**, 055004 (2018).
67. Gelatt, C. D., Williams, A. R. & Moruzzi, V. L. Theory of bonding of transition metals to nontransition metals. *Phys Rev. B* **27**, 2005–2013 (1983).
68. Pasturel, A., Colinet, C. & Hicter, P. Strong chemical interactions in disordered alloys. *Phys. B+C* **132**(2), 177–180 (1985).
69. Hoffmann, R. *Solids and Surfaces. A Chemist's View of Bonding in Extended Structures* (VCH Publishers Inc., 1988).
70. Dronskowski, R. *Computational Chemistry of SOLID State Material* (Wiley-VCH, 2005).
71. Maintz, S., Deringer, V. L., Tchougreeff, A. L. & Dronskowski, R. Analytic projection from plane-wave and PAW wavefunctions and application to chemical-bonding analysis in solids. *J. Comput. Chem.* **34**, 2557–2567 (2013).
72. Dronskowski, R. & Blochl, P. E. Crystal orbital hamilton populations (COHP) Energy-resolved visualization of chemical bonding in solids based on density-functional calculations. *J. Phys. Chem.* **97**, 8617–8624 (1993).
73. Maintz, S., Deringer, V. L., Tchougreeff, A. L. & Dronskowski, R. LOBSTER: A tool to extract chemical bonding from plane-wave based DFT. *J. Comput. Chem.* **37**, 1030–1035 (2016).
74. Arróyave, R. *et al.* Does aluminum play well with others? Intrinsic Al-A alloying behavior in 211/312 MAX phases. *Mater. Res. Lett.* **5**(3), 170–178 (2016).

Acknowledgements

Author contributions

All author contributed equally in conceptualization, design and writing of this manuscript.

Competing interests

The authors declare no competing interests.

Additional information

Correspondence and requests for materials should be addressed to P.S.

Reprints and permissions information is available at www.nature.com/reprints.

Publisher's note Springer Nature remains neutral with regard to jurisdictional claims in published maps and institutional affiliations.